

Insights into a radiology-specialised multimodal large language model with sparse autoencoders

Kenza Bouzid¹ Shruthi Bannur¹ Felix Meissen¹ Daniel Coelho de Castro¹ Anton Schwaighofer¹
Javier Alvarez-Valle¹ Stephanie L. Hyland¹

Abstract

Interpretability can improve the safety, transparency and trust of artificial intelligence (AI) models, which is especially important in healthcare applications where decisions often carry significant consequences. Mechanistic interpretability, particularly through the use of sparse autoencoders (SAEs), offers a promising approach for uncovering human-interpretable features within large transformer-based models. In this study, we apply Matryoshka-SAE to the radiology-specialised multimodal large language model, MAIRA-2, to interpret its internal representations. Using large-scale automated interpretability of the SAE features, we identify a range of clinically relevant concepts—including medical devices (e.g., line and tube placements, pacemaker presence), pathologies such as pleural effusion and cardiomegaly, longitudinal changes and textual features. We further examine the influence of these features on model behaviour through steering, demonstrating directional control over generations with mixed success. Our results reveal practical and methodological challenges, yet they offer initial insights into the internal concepts learned by MAIRA-2—marking a step toward deeper mechanistic understanding and interpretability of a radiology-adapted multimodal large language model, and paving the way for improved model transparency.

We release the trained SAEs and interpretations: <https://huggingface.co/microsoft/maira-2-sae>.

¹Microsoft Research, Health Futures, Cambridge, United Kingdom. Correspondence to: Kenza Bouzid <kenza.bouzid@microsoft.com>, Stephanie Hyland <stephanie.hyland@microsoft.com>.

Workshop on Actionable Interpretability (AIW 2025) at the 42nd International Conference on Machine Learning, Vancouver, Canada. Copyright 2025 by the author(s).

1. Introduction

Recent advancements in automated draft radiology reporting (Bannur et al., 2024; Zhou et al., 2024; Yang et al., 2024; Tu et al., 2024; Chen et al., 2024; Hyland et al., 2023; Wang et al., 2023; Li et al., 2023b) raise the potential of AI systems to reduce radiologist workloads and improve operational efficiency (Yildirim et al., 2024). However, despite strong performance on benchmarks, our understanding of *which* concepts these models have learned—and *how* they use them in the report generation process—remains limited. This lack of interpretability poses challenges in high-stakes domains like healthcare, where trust, transparency, and safety are critical (Quinn et al., 2021).

Mechanistic interpretability aims to address some of these challenges by reverse-engineering the internal computations of neural networks (Elhage et al., 2021; Wang et al., 2022). In this context, SAEs have emerged as a promising tool for inspecting model representations, particularly for large language models (LLMs) (Bricken et al., 2023; Cunningham et al., 2024). By mapping dense model activation vectors to a larger, sparse latent space, it is argued that SAEs can disentangle human-interpretable ‘monosemantic’ features, which may then be labelled at scale using LLMs—a process known as automated interpretability. This approach has enabled insights into model behaviour across various domains, including language (Templeton et al., 2024; Gao et al., 2024; Cunningham et al., 2024; Lieberum et al., 2024; He et al., 2024), vision (Stevens et al., 2025), and proteins (Adams et al., 2025).

Given features of interest, we can intervene on the model’s internal representations to attempt to control its generations according to them (Templeton et al., 2024). This provides both a way to validate the discovered concepts and opens up possibilities for fine-grained control (Stevens et al., 2025; Adams et al., 2025; Zhang et al., 2024). In the context of radiology report generation, such steering—if effective—could be particularly beneficial, for example: guiding the model to omit pathologies for which its performance is unreliable; encouraging more detailed descriptions of medical devices; or preventing the generation of operational text likely to be fabricated (such as notes about physician communication).

In this work, we explore the feasibility of applying SAEs to radiology-focused multimodal large language models (MLLMs). Specifically, we apply Matryoshka-SAE (Bussmann et al., 2025) to MAIRA-2 (Bannur et al., 2024)—one of the most capable publicly available models for grounded and non-grounded chest X-ray (CXR) reporting to date. Leveraging large scale, LLM-based automated interpretability and scoring methods (Paulo et al., 2024), we identify a subset of the internal concepts learned by MAIRA-2, amongst many features that remain uninterpretable. These concepts include classical chest X-rays abnormalities (e.g., atelectasis, cardiomegaly, pleural effusion..), as well as more diverse findings like scoliosis, aortic tortuosity, medical devices, and temporal changes. We use these discovered concepts in steering experiments, observing mixed success across different scenarios. Overall, our findings offer early insights into the internal representations of MAIRA-2, marking a step toward greater interpretability. At the same time, this study highlights several practical and methodological challenges across the pipeline—from SAE training and automated concept discovery to steering—underscoring the complexity of applying mechanistic interpretability methods to models in specialized domains. To foster further research in this direction, we publicly release the trained SAE checkpoints, along with the automated feature interpretations¹.

2. Related work

SAE-based interpretability on language models Templeton et al. (2024) and Gao et al. (2024) performed automated interpretability studies on large proprietary models, which popularised the use of SAEs for this task. Cunningham et al. (2024) quantitatively benchmarked the automatic interpretability success of SAEs against classic unsupervised methods. Other large-scale interpretability efforts (Lieberum et al., 2024; He et al., 2024) have focused on large public models, training suites of SAEs across all layers with a range of hyperparameters and publishing their weights and corresponding auto-interpretations, enabling researchers to build on these often-expensive analyses.

SAEs on multimodal language models Zhang et al. (2024) used SAEs to analyse visual features in a general-domain multimodal model with architecture similar to MAIRA-2, employing a larger multimodal model to automatically explain the learned features. The SAE from Templeton et al. (2024) was trained with language data only, then certain features were shown to also respond to related visual inputs. Lou et al. (2025) investigated the potential of SAE features to guide data selection for improving modality alignment. SAEs were used by Pach et al. (2025) to study representations from a vision encoder then steer a down-

stream language model. Other classic sparse dictionary learning techniques have also been employed to interpret multimodal language models (Parekh et al., 2024).

SAEs in biomedical applications Le et al. (2024) fitted an SAE to a pathology image foundation model, and qualitatively validated several interpretable histological concepts. Abdulaal et al. (2024) applied SAEs to a chest X-ray image encoder, then used automatically generated descriptions of SAE features to compose radiology reports. Simon & Zou (2024) and Adams et al. (2025) have also applied SAEs to interpretation of protein language models, with the former additionally demonstrating steering of protein generation based on interpretable SAE features.

3. Materials and methods

In this section, we describe each element of the experimental pipeline, including the base model and dataset under study, the extraction of internal representations, the SAE used for feature discovery, the procedure for automatically labelling features, and how the feature steering was performed and evaluated. An overview is illustrated in Figure 1.

3.1. MAIRA-2 model

MAIRA-2 (Bannur et al., 2024) is a multimodal language model trained for generating the findings section of radiology reports with or without spatial grounding via bounding boxes. In addition to a frontal CXR image, MAIRA-2 can also optionally ingest: a lateral-view image; indication, technique, and comparison text sections of the current study; and image and report from a prior study of the same patient. This makes it particularly interesting to study since it aligns more closely with real-world clinical workflows than simpler models.

Its architecture is inspired by LLaVA (Liu et al., 2023). Each input image is fed through a radiology-specific encoder (Pérez-García et al., 2025) and a multilayer perceptron adapter to produce 1369 visual token embeddings. These are interleaved with text tokens following a custom prompt template (see example in Table A.1) and given to a 32-layer, 7B-parameter language decoder initialised from Vicuna v1.5 (Chiang et al., 2023). The adapter and language model were trained on a multi-task mix of CXR datasets totalling 511k multimodal samples from 226k unique patients.

3.2. Source dataset

We used MIMIC-CXR (Johnson et al., 2019), a subset of MAIRA-2’s training data, to train SAEs. This dataset consists of paired de-identified chest radiographs and free-text reports. Focusing on the *findings generation* task, we used 158,555 and 7,906 training and validation samples following

¹<https://huggingface.co/microsoft/maira-2-sae>

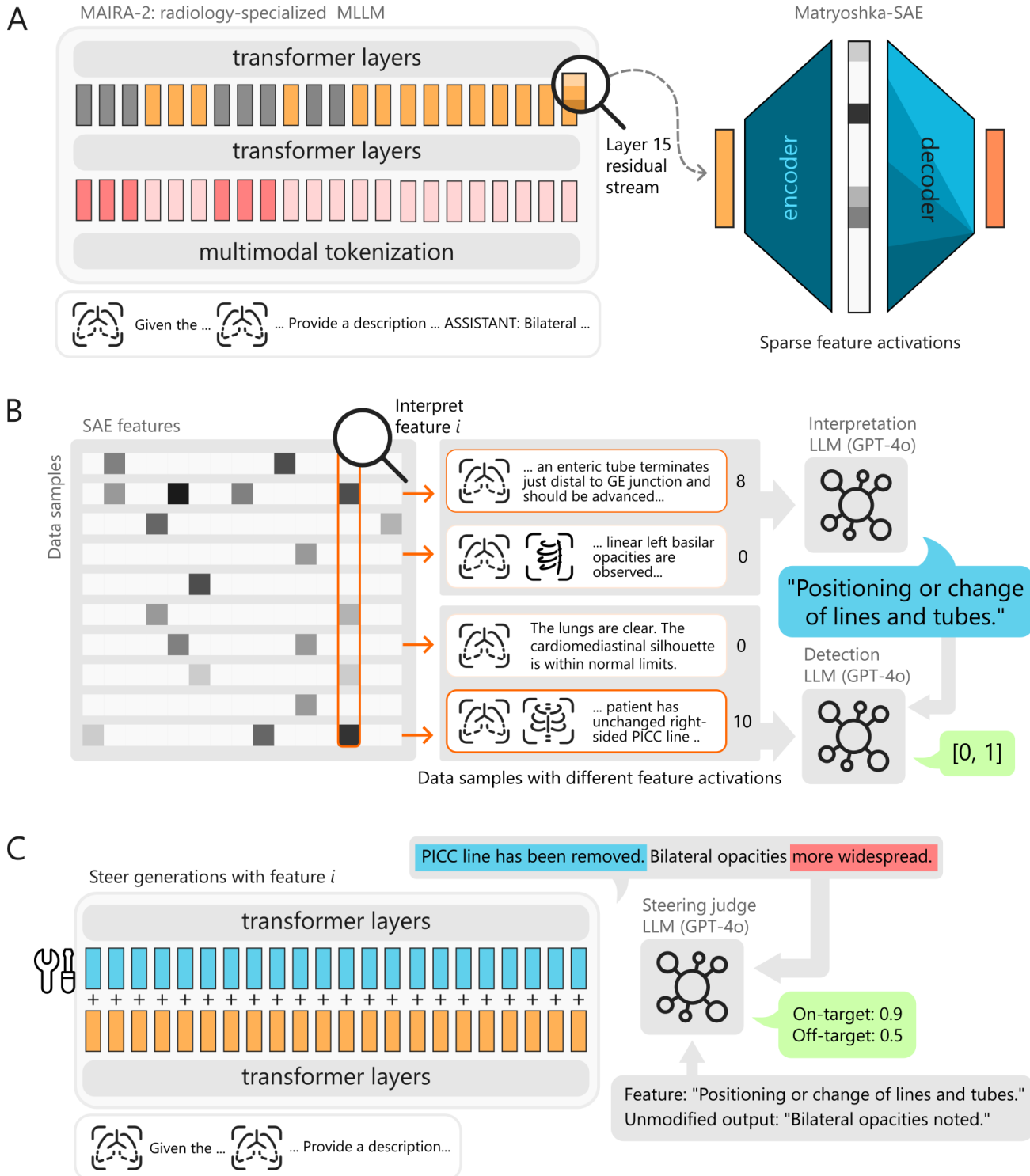


Figure 1. Illustration of the study. **A:** We train a Matryoshka-SAE using the output of the residual stream of MAIRA-2 at layer 15. Multimodal tokenization includes obtaining image tokens from an image encoder. We filter out (grey) token indices corresponding to intermediate image tokens and boilerplate parts of the prompt. **B:** We conduct automated interpretability with LLMs for both deriving interpretations and scoring interpretations, using detection scoring. **C:** We try to steer the generations of MAIRA-2 according to selected features, by adding the corresponding SAE decoder vector to the residual stream at all token positions during each decoding step. Tokenization step omitted for brevity. We evaluate the effectiveness of steering using an LLM to judge on-target and off-target effects.

the same splits and preprocessing in Bannur et al. (2024). We leveraged MAIRA-2’s extended input context capabilities to incorporate all available inputs for a given sample.

3.3. Extraction and filtering of token representations

We used NNsight (Fiotto-Kaufman et al., 2024) for extracting internal representations from the open-source MAIRA-2 model checkpoint². We took the hidden states of the residual stream at the output of the middle layer (#15). This choice was motivated by prior works that suggest that abstract and semantically rich features are most prominent in the middle layers (Templeton et al., 2024; Lad et al., 2024). For each sample, we obtained a sequence of 4096-dimensional token representations, with an average of $3,358 \pm 869$ tokens per sample, reaching a maximum of 5,099 tokens. This included up to three images—each image being represented by 1,369 tokens—along with additional textual context and the ground-truth findings section.

We refined the extracted representations by removing boilerplate and templated subsequences present in the original prompt from Bannur et al. (2024). This type of filtering is commonly applied when analysing internal representations of instruction-tuned language models (Lieberum et al., 2024). We extended this approach to the multimodal setting by retaining only the final image token of each CXR, to avoid the need to interpret an incomplete image. This filtering procedure resulted in 34.7M token representations for training, and 1.7M for validation, substantially reducing the number of tokens to consider. See Table A.1 for an example of token-based representation filtering. In what follows, we refer to these token representations as ‘samples’ as we use them to train and interpret the SAE.

3.4. Sparse autoencoder architecture

We apply techniques from *sparse dictionary learning* (Lee et al., 2006; Cunningham et al., 2024) to disentangle the dense representations of MAIRA-2 into potentially-interpretable sparse features. Specifically, we employ Matryoshka-SAE (Bussmann et al., 2025). By simultaneously training multiple nested autoencoders of increasing size, Matryoshka-SAE is argued to reduce feature splitting and produce more interpretable features.

Formally, given a total dictionary size m and an input $\mathbf{x} \in \mathbb{R}^n$, the Matryoshka-SAE training objective encourages good reconstruction at multiple levels at the same time:

$$\mathcal{L}(\mathbf{x}) = \sum_{m_j \in \mathcal{M}} \underbrace{\|\mathbf{x} - (\mathbf{W}_{1:m_j}^{\text{dec}} \mathbf{f}(\mathbf{x})_{1:m_j} + \mathbf{b}^{\text{dec}})\|_2^2}_{\text{reconstruction using first } m_j \text{ features}} + \alpha \mathcal{L}_{\text{aux}} \quad (1)$$

$$\mathbf{f}(\mathbf{x}) = \sigma(\mathbf{W}^{\text{enc}} \mathbf{x} + \mathbf{b}^{\text{enc}}), \quad (2)$$

²<https://huggingface.co/microsoft/maira-2>

where $1 : m_j$ denotes taking the first m_j elements, \mathcal{M} is the set of nested dictionaries of increasing sizes $m_1 < m_2 < \dots < m_{|\mathcal{M}|} = m$. $\mathbf{W}^{\text{enc}} \in \mathbb{R}^{m \times n}$, $\mathbf{b}^{\text{enc}} \in \mathbb{R}^m$ are the encoder matrix and bias, $\mathbf{W}^{\text{dec}} \in \mathbb{R}^{n \times m}$, $\mathbf{b}^{\text{dec}} \in \mathbb{R}^n$ are the decoder matrix and bias. Similar to Bussmann et al. (2025), we use BatchTopK (Bussmann et al., 2024) as activation function σ (with slight abuse of notation), which builds on TopK (Gao et al., 2024) to enforce an average sparsity of k active features across a batch of size b . Finally, \mathcal{L}_{aux} is the auxiliary loss suggested in Gao et al. (2024) to reduce dead neurons, further described in Appendix A.3. In what follows, f_i refers to the i ’th feature in the sparse latent space of the SAE, with $i \in [0, m - 1]$.

3.5. SAE training

We relied on the open-source `dictionary_learning` repository³ (Marks et al., 2024) to train the SAEs used in this study. We rescaled all token representations similarly to Gao et al. (2024), with a normalization factor of 22.34, computed from the full training set as the mean ℓ_2 norm of the representations. We benchmarked several SAE architectures, including TopKSAE (Gao et al., 2024), BatchTopKSAE (Bussmann et al., 2024), and Matryoshka-SAE (Bussmann et al., 2025), and found that the latter achieved the best reconstruction performance in this context. The width of SAEs is commonly specified as a factor of the hidden dimensionality of the base model (4096 for MAIRA-2). We experimented with various expansion factors $\text{ef} \in \{2, 4, 8, 16\}$. Although $\text{ef} = 16$ achieved the best reconstruction performance, we selected $\text{ef} = 4$ as a trade-off between reconstruction quality, sparsity, and the computational cost of the downstream auto-interpretation pipeline that requires extensive LLM API calls. We also tested multiple values of the sparsity parameter $k \in \{32, 64, 128, 256\}$, with $k = 256$ producing the most favourable results in terms of reconstruction fidelity and lowest number of dead features, consistent with the settings in Zhang et al. (2024). Unless stated otherwise, all downstream results are reported using Matryoshka-SAE with $\text{ef} = 4$ and $k = 256$, resulting in 16,384 features. A full list of hyperparameters is provided in Table A.2.

3.6. Automated interpretation of SAE features

To identify which SAE features correspond to human-interpretable concepts, we follow prior work in interpreting features at scale with an automated, LLM-based pipeline (Paulo et al., 2024; Bricken et al., 2023; Bills et al., 2023).

For each feature, we randomly collect samples that do not activate it ($f_i(\mathbf{x}) = 0$) and an equal number with activation strength in the top observed decile. We found this sampling strategy superior to the fully stratified sampling done in

³https://github.com/saprmarks/dictionary_learning

earlier work (Paulo et al., 2024). We then query an LLM (GPT-4o version 2024-11-20) to produce an interpretation of the observed activation patterns. Although MAIRA-2 consumes interleaved images and text, we provide our interpretation LLM with text inputs only, because the reliability of the generalist GPT-4* series on CXR image understanding has been questioned (Yan et al., 2024; Jiang et al., 2024).

We score the quality of these interpretations following the detection approach from Paulo et al. (2024), which scores a (textual) feature interpretation by how well it can be used to predict whether that feature will be active on a new sample, again using an LLM. Where possible, we balance the number of positive and negative samples⁴ and report detection F_1 on the evaluation set as a measure of feature interpretability. For scoring we sample from the top quintile and again hold non-activating samples as the balanced ‘negatives’.

We use 50 data examples per feature to derive an interpretation, and 200 (non-overlapping) examples to score interpretation quality. We source these examples from a set of 500,000 randomly selected samples from the dataset used to train the SAE. We generate and score interpretations for every feature in the SAE for which it is possible to collect samples as prescribed above, resulting in interpretations for 99.5% (16,299) of the 16,384 features. Further details on automated interpretation, including LLM prompts, are in Appendices C.2 and C.3.

3.7. Steering

SAE features can be used to manipulate a model’s output towards or away from desired concepts in a process called steering (Templeton et al., 2024; Adams et al., 2025; Zhang et al., 2024). To steer model generations using a single SAE feature f_i , we extract the corresponding column $\mathbf{W}_i^{\text{dec}}$ from the SAE decoder matrix as a steering vector. This vector is multiplied by a coefficient α and added at each decoding step to the hidden states for every token in the sequence—whether in the prompt or generated tokens (Turner et al., 2023; Li et al., 2023a; Durmus et al., 2024). By intervening on the hidden states in this manner, we expect the model generations to introduce or emphasise content associated with the targeted concept, reflecting an induced high activation of that feature. In contrast, applying negative coefficients is expected to de-emphasise, remove, or even invert the corresponding concept in the model generation.

Finding the right steering coefficient α is non-trivial. After initial experiments with a wide range of steering coefficients ($\alpha \in \{1, 2.5, 5, 10, 15, 25, 50, 100\}$), we chose $\alpha = 10$ for positive and $\alpha = -10$ for negative steering as they strike a

⁴It was not always possible to find 100 positive examples for a given feature, resulting in an imbalanced evaluation set. However, we did not observe a correlation between imbalance and F_1 .

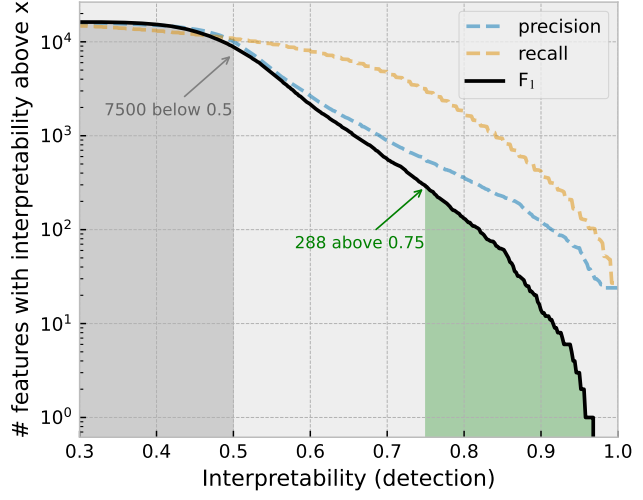


Figure 2. Interpretable features exist, but are rare. Using detection F_1 on the evaluation set as a measure of interpretability, we show that from 16,384 features, 288 (1.8%) score above 0.75, whereas 7,500 (46%) score below 0.5 (random performance for a balanced evaluation set).

good balance between the appearance of noticeable targeted changes while remaining in-distribution.

3.8. Evaluating steering success

Successful steering should modify only the concept of interest while keeping the rest unchanged. We therefore evaluate the effectiveness of steering using two dimensions: *on-target* changes refer to modifications directly related to the concept of interest, while *off-target* changes are all other significant alterations of the content of the generated report. Both dimensions of change are measured in comparison between the reports generated with and without the steering intervention. To enable large-scale evaluation of steering success of multiple concepts, we use an LLM-as-a-judge approach similar to Wu et al. (2025). The LLM is prompted to output on-target and off-target scores from 0 to 1, where higher scores correspond to stronger changes. More details about the LLM judge are in Appendix D.

4. Findings

4.1. MAIRA-2 contains interpretable features

Figure 2 shows the distribution of detection F_1 across the 16,384 features in our SAE. With 7,500 (46%) features below 0.5, this illustrates that many features are not interpretable by our automated pipeline. There do however exist consistently interpretable features, with 288 (1.8%) exhibiting F_1 above 0.75. We observe consistently higher recall than precision, indicating that feature descriptions

tend towards being non-specific.

We observe that highly interpretable features tend to pertain to the presence of abnormal findings (f_{1336} , $F_1 = 0.89$: ‘*Aortic tortuosity or calcification identified in chest imaging.*’), changes especially of medical lines and tubes (f_{11240} , $F_1 = 0.96$: ‘*Descriptions of findings related to chest tube placement or removal.*’), and reporting style (f_{12106} , $F_1 = 0.93$: ‘*Use of ‘however’ in clinical findings indicating possible issues needing further investigation.*’).

Features with low detection F_1 are most commonly ascribed generic descriptions of the task of radiology reporting emphasising comparison with prior imaging (f_{730} and 16 others, $F_1 = 0.50$: ‘*Comparative analysis of current and prior imaging findings.*’, f_{12117} and 5 others, $F_1 = 0.40$, ‘*Comparison of current imaging findings to prior studies.*’), and less frequently references to the instruction given to MAIRA-2 (f_{2653} , $F_1 = 0.42$, ‘*Provide findings description in comparison with prior images.*’), or pathological changes (f_{10005} , $F_1 = 0.43$, ‘*Enlargement of cardiac silhouette often with pulmonary vascular changes.*’).

Even among highly interpretable features, we observe a degree of repetition in feature descriptions: of the 61 features with F_1 above 0.85, we observe seven instances of apparent repetition. For example, f_{1374} and f_{6105} are ‘*Presence of atelectasis in imaging findings.*’ and ‘*Mentions and descriptions of atelectasis*’ respectively, and f_{13515} and f_{13911} are both described as ‘*Elevation of the hemidiaphragm*’.

4.2. Steering success depends on the feature

In this section, we evaluate to what extent the SAE features can be used to effectively steer the model generation into desired directions. Figure 3 shows the steering performance across a set of highly interpretable features on the full validation set of 7,906 CXR studies. The LLM-based steering evaluation produces two metrics: an *on-target score* and an *off-target score*. Based on these metrics, we stratify the results into four disjoint cases: (1) only on-target changes were observed; (2) both on-target and off-target changes; (3) only off-target changes; and (4) no observable changes occurred following steering. We show examples from each category in Table 1. We describe the process of selecting features for steering and additional results and examples for both positive and negative steering in Appendix E.

Overall, feature steering produces more off-target changes than on-target changes. Purely on-target changes are relatively rare, with the highest observed proportion being 11.3%, seen in f_{10709} . An example of such a case is shown for f_{1599} in the top row of Table 1, where the steered generation effectively removed all comparisons to prior studies.

More commonly, on-target effects are accompanied by varying degrees of off-target changes. In f_{6412} , for example,

27.4% of cases exhibit both on- and off-target changes. While some of these off-target changes reflect underlying correlations in the dataset—for example in f_{6412} in Table 1, where the output includes *atelectasis* alongside *pleural effusion*, consistent with known clinical correlations—most off-target changes are not due to such causal relationships. In many cases, off-target changes are seen when the original report is non-specific (For example, “No significant interval change”) while the steered generation is more descriptive, leading to large off-target changes due to the discrepancy.

In most cases, steering leads predominantly to off-target effects. Extreme cases include, but are not limited to, f_{11509} , f_{10643} , and f_{13506} where more than 50% of the steered samples contain off-target changes despite showing almost no on-target changes. The corresponding example for f_{10643} in Table 1 adds a right apical pneumothorax, a left pleural effusion, and tips descriptions, none of which are directly related to the feature’s description of ‘*Immediate notifications of findings by telephone upon discovery.*’

In approximately 35% of cases across all features, steering leads to no observable changes.

Interestingly, we observe a strong correlation in the on-target effects between steering features with a positive and with a negative coefficient α (Spearman’s $\rho = 0.90$, $p \leq 0.05$, $n = 67$). The correlation is also present for off-target effects, although less pronounced (Spearman’s $\rho = 0.71$, $p \leq 0.05$, $n = 67$). We also observe a correlation between the activation frequency of a feature and its on-target score (Spearman’s $\rho = 0.40$, $p \leq 0.05$, $n = 50$) for features with $F_1 > 0.85$. We do not observe a significant correlation of the activation frequency with off-target scores.

This section leaves us with two main observations: (1) the success of feature steering highly depends on the selected feature and the steered report, and (2) even when successful, feature steering regularly produces more off-target effects than on-target effects.

5. Discussion and conclusion

Motivated by the success of SAE-based approaches for the interrogation of LLMs, in this work we investigated the radiology-specialized MLLM Bannur et al. (MAIRA-2; 2024) using Matryoshka-SAE (Bussmann et al., 2025). We based our automated interpretability and scoring pipeline on an established approach (Paulo et al., 2024), with some modifications specific to the radiology domain. We then explored the extent to which MAIRA-2 can be steered using the discovered interpretable features.

We found a small set of highly interpretable SAE features, representing a variety of concepts pertinent to radiology reporting, and often with more granularity than existing

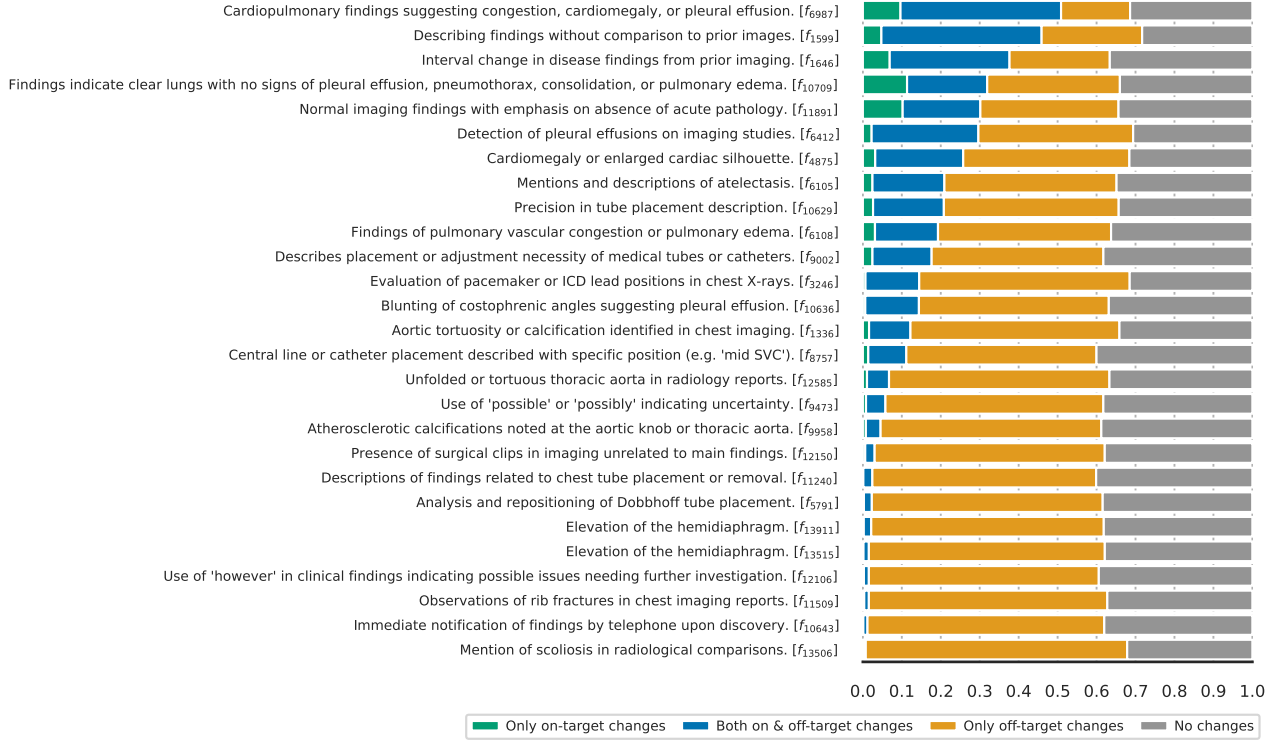


Figure 3. On-target and off-target effects of steering features f_i with $\alpha = 10$. The scores of the LLM judge are binarized at 0.1 and the bars show the proportion of samples where steering led only to on-target changes, only to off-target changes, both, or none at all. Results are shown for the full validation set including 7,906 studies.

concept categories such as the CheXpert classes (Irvin et al., 2019). Among these highly interpretable features, we observed some repeated or similar feature descriptions, which may be evidence for feature composition (Anders et al., 2024; Wattenberg & Viégas, 2024) or splitting (Bricken et al., 2023). Almost half of the SAE features were found not to be interpretable by our pipeline. It is difficult to establish the base rate of ‘interpretable’ features discovered in SAE analyses as most prior work reports on subsets of features (Paulo et al., 2024; Bussmann et al., 2025; Minder et al., 2025; Templeton et al., 2024) or subsets of evaluation samples (Mudide et al., 2024), whereas here we report scores for almost all SAE features.

Nonetheless, it may be possible to uncover more interpretable features in MAIRA-2 with improvements in automated interpretability, for example making use of a radiology-adept MLLM to more comprehensively capture imaging content, by further improving the selection of dataset exemplars (e.g. using ‘hard’ negatives as in Minder et al. (2025)), or by actively seeking ‘output’ features (Paulo et al., 2024; Gur-Arieh et al., 2025) through an intervention-based interpretation pipeline (Shaham et al., 2024). However, given our specialised domain, we are limited in the set of models available for e.g. CXR visual question-answering,

or generation of counterfactual examples.

Our study discovered two recurring patterns related to steering success. First, we found a significant correlation between the activation frequency of features in the training dataset and steering success for highly interpretable features. Given that the training data in this study was a subset of MAIRA-2’s training data, we hypothesise that frequently activating features are well learned and better represented in the language model’s latent space—which in return is the cause for the high steering success of such features. Second, features that are highly steerable in the positive direction also show good steering performance in the negative direction and vice versa. This suggests that the learned features retain their approximate linearity far below the point where they usually activate. Other recent studies on steering LLMs with hand-picked SAE features also found disproportionately many failure cases, but could not provide an empirical explanation (Durmus et al., 2024; O’Brien et al., 2024). This also relates to the comprehensive steering benchmarking study from Wu et al. (2025), wherein almost all steering methods (including SAE-based) dramatically underperformed prompting and fine-tuning.

Alongside low steering success, we also observed adverse

Table 1. Examples of steered reports including LLM-based evaluation. Following the colouring from Figure 3, on-target changes between the original and the steered report are highlighted in green, and off-target effects in orange.

Only on-target changes	
Feature	f_{1599} , $F_1 = 0.79$: ‘Describing findings without comparison to prior images.’
Original	Compared with the prior study, lung volumes are lower, causing bronchovascular crowding. However, no focal consolidation, pleural effusion, or pneumothorax. Cardiomedastinal and hilar silhouettes are unchanged.
Steered $\alpha = 10$	Lung volumes are low, causing bronchovascular crowding. No focal consolidation, pleural effusion, or pneumothorax. Cardiomedastinal and hilar silhouettes are unremarkable.
Scores	on-target score=1.0 off-target score=0.0
Both on- and off-target changes	
Feature	f_{6412} , $F_1 = 0.84$: ‘Detection of pleural effusions on imaging studies.’
Original	The heart size is normal. The mediastinal and hilar contours are unremarkable. The pulmonary vascularity is normal. Patchy ill-defined opacity is noted within the left lung base, which may represent an area of developing infection. No pleural effusion or pneumothorax is present. There are no acute osseous abnormalities.
Steered $\alpha = 10$	The heart size is normal. The mediastinal and hilar contours are unremarkable. The pulmonary vascularity is normal. There is a small left pleural effusion. Minimal streaky opacity in the left lung base may reflect atelectasis, though infection cannot be completely excluded. There is no pneumothorax. No acute osseous abnormality is seen.
Scores	on-target score=1.0 off-target score=0.2
Only off-target changes	
Feature	f_{10643} , $F_1 = 0.86$: ‘Immediate notification of findings by telephone upon discovery.’
Original	Since –, small right pleural effusion is unchanged, right pleural catheter is in unchanged position. The lungs are clear. The cardiomedastinal silhouette, hilar contours, and pleural surfaces are normal. No pneumothorax.
Steered $\alpha = 10$	Since –, a right pleural drainage catheter is in place. A small right apical pneumothorax is seen. A small right pleural effusion is seen. A left pleural effusion is small. The lungs are clear. The heart size is normal. Tips in the esophagus are noted.
Scores	on-target score=0.1 off-target score=0.7

effects from steering, causing sometimes clinically significant changes unrelated to the concept of interest, such as the confabulation or omission of findings. Compared to generalist models used by Durmus et al. (2024) and O’Brien et al. (2024), the nature of our application both required and allowed us to perform a more principled evaluation of the side-effects of steering than these works, which revealed that these off-target changes often exceed those observed along the concept dimension.

The reasons for the low steering success and the large adverse effects remain speculative but could be rooted in limitations of the SAEs used for concept discovery, of the steering method, or of the automated feature interpretation and steering evaluation pipelines. For example, quantitatively measuring on-target effects is challenging when a concept is already present. This is, for example, observed for f_{6412} : attempting to add more pleural effusions to a report that already describes bilateral pleural effusions should rightfully result in no change compared to the original output. This effect is especially relevant in negative steering since most concepts are already absent in the majority of samples. More fundamentally, it is possible that the SAE features themselves are not well disentangled (cf. feature splitting/absorption/composition; Bricken et al., 2023; Chanin et al.,

2024; Anders et al., 2024), or that representations of concepts of interest are significantly nonlinear in MAIRA-2 (Park et al., 2024). Some of the problems above could be alleviated by more informed steering methods that would especially incorporate knowledge about *which* tokens to modify and *how much*.

In conclusion, this study provides early insights into the inner workings of a radiology-specialised MLLM, while also highlighting various practical and technical challenges in applying mechanistic interpretability methods to domain-specific models. Notably:

- We identify a subset of the internal concepts in MAIRA-2 that are often more fine-grained than existing findings labels for CXR reports, despite many features remaining uninterpretable.
- While concept steering shows potential, its effectiveness varies considerably by feature and case—highlighting the need for further investigation.
- These findings lay a foundation for more transparent, interpretable, and controllable radiology MLLMs, and support continued research through the planned release of the SAE checkpoint and automated interpretations.

By releasing⁵ the trained SAEs and LLM-generated interpretations for all features, we hope to facilitate further research into the application of mechanistic interpretability to specialised multimodal models such as MAIRA-2.

Impact Statement

This paper focuses on approaches to understand the internal representations of a radiology-adapted MLLM and potentially control its behaviour through steering. The use of MLLM on medical data can have positive or negative impacts depending on the context of use since such models can generate incorrect or misleading outputs. Extracting interpretable features from model internals may provide model builders a route towards designing safer or more effective models. Steering could provide an additional mechanism by which models can be controlled, either to enhance or suppress unsafe or other undesirable behaviours.

References

Abdulaal, A., Fry, H., Montaña-Brown, N., Ijishakin, A., Gao, J., Hyland, S., Alexander, D. C., and Castro, D. C. An X-ray is worth 15 features: Sparse autoencoders for interpretable radiology report generation. *arXiv preprint arXiv:2410.03334*, 2024.

Adams, E., Bai, L., Lee, M., Yu, Y., and AlQuraishi, M. From Mechanistic Interpretability to Mechanistic Biology: Training, Evaluating, and Interpreting Sparse Autoencoders on Protein Language Models, February 2025. URL <https://www.biorxiv.org/content/10.1101/2025.02.06.636901v1>. Pages: 2025.02.06.636901 Section: New Results.

Anders, E., Neo, C., Hoelscher-Obermaier, J., and Howard, J. N. Sparse autoencoders find composed features in small toy models, 2024. URL <https://www.lesswrong.com/posts/a5wwqza2cY3W7L9cj>.

Bannur, S., Bouzid, K., Castro, D. C., Schwaighofer, A., Bond-Taylor, S., Ilse, M., Pérez-García, F., Salvatelli, V., Sharma, H., Meissen, F., Ranjit, M., Srivastav, S., Gong, J., Falck, F., Oktay, O., Thieme, A., Lungren, M. P., Wetscherek, M. T., Alvarez-Valle, J., and Hyland, S. L. MAIRA-2: Grounded Radiology Report Generation, June 2024. URL <http://arxiv.org/abs/2406.04449>.

Bills, S., Cammarata, N., Mossing, D., Tillman, H., Gao, L., Goh, G., Sutskever, I., Leike, J., Wu, J., and Saunders, W. Language models can explain neurons in language models. <https://openaipublic.blob.core.windows.net/neuron-explainer/paper/index.html>, 2023.

Bricken, T., Templeton, A., Batson, J., Chen, B., Jermyn, A., Conerly, T., Turner, N., Anil, C., Denison, C., Askell, A., Lasenby, R., Wu, Y., Kravec, S., Schiefer, N., Maxwell, T., Joseph, N., Hatfield-Dodds, Z., Tamkin, A., Nguyen, K., McLean, B., Burke, J. E., Hume, T., Carter, S., Henighan, T., and Olah, C. Towards monosemanticity: Decomposing language models with dictionary learning. *Transformer Circuits Thread*, 2023. URL <https://transformer-circuits.pub/2023/monosemantic-features/index.html>.

Bussmann, B., Leask, P., and Nanda, N. BatchTopK sparse autoencoders. *arXiv preprint arXiv:2412.06410*, 2024.

Bussmann, B., Nabeshima, N., Karvonen, A., and Nanda, N. Learning Multi-Level Features with Matryoshka Sparse Autoencoders, March 2025. URL <http://arxiv.org/abs/2503.17547>. arXiv:2503.17547 [cs].

Chanin, D., Wilken-Smith, J., Dulka, T., Bhatnagar, H., and Bloom, J. I. A is for absorption: Studying feature splitting and absorption in sparse autoencoders. In *NeurIPS 2024 Workshop on Interpretable AI*, December 2024. URL <https://openreview.net/forum?id=Wzav8fesTL>.

Chen, Z., Varma, M., Delbrouck, J.-B., Paschali, M., Blanke-meier, L., Van Veen, D., Valanarasu, J. M. J., Youssef, A., Cohen, J. P., Reis, E. P., et al. CheXagent: Towards a foundation model for chest x-ray interpretation. *arXiv preprint arXiv:2401.12208*, 2024.

Chiang, W.-L., Li, Z., Lin, Z., Sheng, Y., Wu, Z., Zhang, H., Zheng, L., Zhuang, S., Zhuang, Y., Gonzalez, J. E., Stoica, I., and Xing, E. P. Vicuna: An open-source chatbot impressing GPT-4 with 90%* ChatGPT quality, March 2023. URL <https://lmsys.org/blog/2023-03-30-vicuna/>.

Cunningham, H., Ewart, A., Riggs, L., Huben, R., and Sharkey, L. Sparse autoencoders find highly interpretable features in language models. In *The Twelfth International Conference on Learning Representations*, 2024. URL <https://openreview.net/forum?id=F76bwRSLeK>.

Durmus, E., Tamkin, A., Clark, J., Wei, J., Marcus, J., Batson, J., Handa, K., Lovitt, L., Tong, M., McCain, M., Rausch, O., Huang, S., Bowman, S., Ritchie, S., Henighan, T., and Ganguli, D. Evaluating feature steering: A case study in mitigating social biases, 2024. URL <https://anthropic.com/research/evaluating-feature-steering>.

Elhage, N., Nanda, N., Olsson, C., Henighan, T., Joseph, N., Mann, B., Askell, A., Bai, Y., Chen, A., Conerly, T., et al. A mathematical framework for transformer circuits. *Transformer Circuits Thread*, 2021.

⁵<https://huggingface.co/microsoft/maira-2-sae>

Fiotto-Kaufman, J., Loftus, A. R., Todd, E., Brinkmann, J., Juang, C., Pal, K., Rager, C., Mueller, A., Marks, S., Sharma, A. S., et al. NNsight and NDIF: Democratizing access to foundation model internals. *arXiv preprint arXiv:2407.14561*, 2024.

Gao, L., la Tour, T. D., Tillman, H., Goh, G., Troll, R., Radford, A., Sutskever, I., Leike, J., and Wu, J. Scaling and evaluating sparse autoencoders, June 2024. URL <http://arxiv.org/abs/2406.04093>. arXiv:2406.04093 [cs].

Gur-Arieh, Y., Mayan, R., Agassy, C., Geiger, A., and Geva, M. Enhancing automated interpretability with output-centric feature descriptions. *arXiv preprint arXiv:2501.08319*, 2025.

He, Z., Shu, W., Ge, X., Chen, L., Wang, J., Zhou, Y., Liu, F., Guo, Q., Huang, X., Wu, Z., Jiang, Y.-G., and Qiu, X. Llama Scope: Extracting millions of features from Llama-3.1-8B with sparse autoencoders, 2024. URL <https://arxiv.org/abs/2410.20526>.

Hyland, S. L., Bannur, S., Bouzid, K., Castro, D. C., Ranjit, M., Schwaighofer, A., Pérez-García, F., Salvatelli, V., Srivastav, S., Thieme, A., et al. MAIRA-1: A specialised large multimodal model for radiology report generation. *arXiv:2311.13668*, 2023. URL <https://arxiv.org/abs/2311.13668>.

Irvin, J., Rajpurkar, P., Ko, M., Yu, Y., Ciurea-Ilcus, S., Chute, C., Marklund, H., Haghgoo, B., Ball, R., Shpanskaya, K., et al. CheXpert: A large chest radiograph dataset with uncertainty labels and expert comparison. In *Proceedings of the AAAI conference on artificial intelligence*, volume 33, pp. 590–597, 2019.

Jiang, Y., Chen, C., Nguyen, D., Mervak, B. M., and Tan, C. GPT-4V cannot generate radiology reports yet. *ArXiv*, abs/2407.12176, 2024. URL <https://api.semanticscholar.org/CorpusID:271244474>.

Johnson, A. E. W., Pollard, T. J., Berkowitz, S. J., Mark, R. G., and Horng, S. MIMIC-CXR database (version 2.0.0). PhysioNet, 2019.

Lad, V., Gurnee, W., and Tegmark, M. The remarkable robustness of LLMs: Stages of inference? *arXiv preprint arXiv:2406.19384*, 2024.

Le, N. M., Patel, N., Shen, C., Martin, B., Eng, A., Shah, C., Grullon, S., and Juyal, D. Learning biologically relevant features in a pathology foundation model using sparse autoencoders. In *NeurIPS 2024 Workshop on Advancements In Medical Foundation Models*, December 2024. URL <https://openreview.net/forum?id=daV16mhUBd>.

Lee, H., Battle, A., Raina, R., and Ng, A. Efficient sparse coding algorithms. *Advances in neural information processing systems*, 19, 2006.

Li, K., Patel, O., Viégas, F., Pfister, H., and Wattenberg, M. Inference-time intervention: Eliciting truthful answers from a language model. *Advances in Neural Information Processing Systems*, 36:41451–41530, 2023a.

Li, M., Lin, B., Chen, Z., Lin, H., Liang, X., and Chang, X. Dynamic graph enhanced contrastive learning for chest x-ray report generation. In *Proceedings of the IEEE/CVF Conference on Computer Vision and Pattern Recognition*, pp. 3334–3343, 2023b.

Lieberum, T., Rajamanoharan, S., Conmy, A., Smith, L., Sonnerat, N., Varma, V., Kramár, J., Dragan, A., Shah, R., and Nanda, N. Gemma Scope: Open sparse autoencoders everywhere all at once on Gemma 2. *arXiv preprint arXiv:2408.05147*, 2024.

Liu, H., Li, C., Wu, Q., and Lee, Y. J. Visual instruction tuning. In *Advances in Neural Information Processing Systems*, volume 36, pp. 34892–34916, 2023.

Lou, H., Li, C., Ji, J., and Yang, Y. SAE-V: Interpreting Multimodal Models for Enhanced Alignment, February 2025. URL <http://arxiv.org/abs/2502.17514>. arXiv:2502.17514 [cs].

Marks, S., Karvonen, A., and Mueller, A. https://github.com/saprmarks/dictionary_learning, 2024.

Minder, J., Dumas, C., Juang, C., Chugtai, B., and Nanda, N. Robustly identifying concepts introduced during chat fine-tuning using crosscoders. *arXiv preprint arXiv:2504.02922*, 2025.

Mudide, A., Engels, J., Michaud, E. J., Tegmark, M., and de Witt, C. S. Efficient dictionary learning with switch sparse autoencoders. *arXiv preprint arXiv:2410.08201*, 2024.

O’Brien, K., Majercak, D., Fernandes, X., Edgar, R., Chen, J., Nori, H., Carignan, D., Horvitz, E., and Poursabzi-Sangde, F. Steering language model refusal with sparse autoencoders. *arXiv preprint arXiv:2411.11296*, 2024.

Pach, M., Karthik, S., Bouniot, Q., Belongie, S., and Akata, Z. Sparse Autoencoders Learn Monosemantic Features in Vision-Language Models, April 2025. URL <http://arxiv.org/abs/2504.02821>. arXiv:2504.02821 [cs].

Parekh, J., Khayatan, P., Shukor, M., Newson, A., and Cord, M. A concept-based explainability framework for large multimodal models. *Advances in Neural Information Processing Systems*, 37:135783–135818, 2024.

Park, K., Choe, Y. J., and Veitch, V. The linear representation hypothesis and the geometry of large language models. In *Proceedings of the 41st International Conference*

on Machine Learning, pp. 39643–39666. PMLR, July 2024. URL <https://proceedings.mlr.press/v235/park24c.html>.

Paulo, G., Mallen, A., Juang, C., and Belrose, N. Automatically Interpreting Millions of Features in Large Language Models, December 2024. URL <http://arxiv.org/abs/2410.13928>. arXiv:2410.13928 [cs].

Pérez-García, F., Sharma, H., Bond-Taylor, S., Bouzid, K., Salvatelli, V., Ilse, M., Bannur, S., Castro, D. C., Schwaighofer, A., Lungren, M. P., et al. Exploring scalable medical image encoders beyond text supervision. *Nature Machine Intelligence*, 7:119–130, 2025. doi: 10.1038/s42256-024-00965-w.

Quinn, T. P., Senadeera, M., Jacobs, S., Coghlan, S., and Le, V. Trust and medical ai: the challenges we face and the expertise needed to overcome them. *Journal of the American Medical Informatics Association*, 28(4):890–894, 2021.

Shaham, T. R., Schwettmann, S., Wang, F., Rajaram, A., Hernandez, E., Andreas, J., and Torralba, A. A multimodal automated interpretability agent. In *Forty-first International Conference on Machine Learning*, 2024.

Simon, E. and Zou, J. InterPLM: Discovering Interpretable Features in Protein Language Models via Sparse Autoencoders, November 2024. URL <https://www.biorxiv.org/content/10.1101/2024.11.14.623630v1>. Pages: 2024.11.14.623630 Section: New Results.

Stevens, S., Chao, W.-L., Berger-Wolf, T., and Su, Y. Sparse autoencoders for scientifically rigorous interpretation of vision models. *arXiv preprint arXiv:2502.06755*, 2025.

Templeton, A., Conerly, T., Marcus, J., Lindsey, J., Bricken, T., Chen, B., Pearce, A., Citro, C., Ameisen, E., Jones, A., Cunningham, H., Turner, N. L., McDougall, C., MacDiarmid, M., Freeman, C. D., Sumers, T. R., Rees, E., Batson, J., Jermyn, A., Carter, S., Olah, C., and Henighan, T. Scaling monosemanticity: Extracting interpretable features from Claude 3 Sonnet. *Transformer Circuits Thread*, 2024. URL <https://transformer-circuits.pub/2024/scaling-monosemanticity/index.html>.

Tu, T., Azizi, S., Driess, D., Schaeckermann, M., Amin, M., Chang, P.-C., Carroll, A., Lau, C., Tanno, R., Ktena, I., Palepu, A., Mustafa, B., Chowdhery, A., Liu, Y., Kornblith, S., Fleet, D., Mansfield, P., Prakash, S., Wong, R., Virmani, S., et al. Towards generalist biomedical AI. *NEJM AI*, 1(3):A1oa2300138, February 2024. doi: 10.1056/A1oa2300138.

Turner, A. M., Thiergart, L., Leech, G., Udell, D., Vazquez, J. J., Mini, U., and MacDiarmid, M. Steering language models with activation engineering. *arXiv preprint arXiv:2308.10248*, 2023.

Wang, K., Variengien, A., Conmy, A., Shlegeris, B., and Steinhardt, J. Interpretability in the wild: a circuit for indirect object identification in GPT-2 small. *arXiv preprint arXiv:2211.00593*, 2022.

Wang, Z., Liu, L., Wang, L., and Zhou, L. Metransformer: Radiology report generation by transformer with multiple learnable expert tokens. In *Proceedings of the IEEE/CVF Conference on Computer Vision and Pattern Recognition*, pp. 11558–11567, 2023.

Wattenberg, M. and Viégas, F. B. Relational composition in neural networks: A survey and call to action, 2024. URL <https://arxiv.org/abs/2407.14662>.

Wu, Z., Arora, A., Geiger, A., Wang, Z., Huang, J., Jurafsky, D., Manning, C. D., and Potts, C. AxBench: Steering LLMs? Even Simple Baselines Outperform Sparse Autoencoders, March 2025. URL <http://arxiv.org/abs/2501.17148>. arXiv:2501.17148 [cs].

Yan, Q., He, X., Yue, X., and Wang, X. E. Worse than random? an embarrassingly simple probing evaluation of large multimodal models in medical VQA. *ArXiv*, abs/2405.20421, 2024. URL <https://api.semanticscholar.org/CorpusID:270199350>.

Yang, L., Xu, S., Sellergren, A., Kohlberger, T., Zhou, Y., Ktena, I., Kiraly, A., Ahmed, F., Hormozdiari, F., Jaroensri, T., et al. Advancing multimodal medical capabilities of Gemini. *arXiv preprint arXiv:2405.03162*, 2024.

Yildirim, N., Richardson, H., Wetscherek, M. T., Bajwa, J., Jacob, J., Pinnock, M. A., Harris, S., Coelho De Castro, D., Bannur, S., Hyland, S., et al. Multimodal healthcare AI: Identifying and designing clinically relevant vision-language applications for radiology. In *Proceedings of the 2024 CHI Conference on Human Factors in Computing Systems*, pp. 1–22, 2024.

Zhang, K., Shen, Y., Li, B., and Liu, Z. Large Multimodal Models Can Interpret Features in Large Multimodal Models, November 2024. URL <http://arxiv.org/abs/2411.14982>. arXiv:2411.14982 [cs].

Zhou, H.-Y., Adithan, S., Acosta, J. N., Topol, E. J., and Rajpurkar, P. A generalist learner for multifaceted medical image interpretation. *arXiv preprint arXiv:2405.07988*, 2024.

A. Additional experimental setup details

A.1. Representation filtering

Table A.1 shows the effect of the token-based representation filtering, keeping only the most relevant tokens for the task at hand. We discard any fixed segments from the original prompt template: the system prompt, beginning- and end-of-sequence tokens, the chat template delimiters, and the fixed parts of the instruction. We choose to depict an example that include all three possible CXR image views as a comprehensive representation of the filtering.

Table A.1. Example of token based representations filtering, including a frontal, lateral and prior image. In the filtered prompt, we indicate the indices of the tokens which were kept in square brackets. We further extract the message type ('human' or 'assistant') and the content type ('str' or 'image').

Original Prompt	Filtered Prompt
<pre><s>, _You, _are, _an, _expert, _radi, ology, _assistant, _task, ed, _with, _interpre, ting, _a, _ch, est, _X, -, _ray, _study, ., _, _US, ER, :, _, _Given, _the, _current, _front, al, _image, <image>x1369, _the, _current, _later, al, _image, <lat_image>x1369, _and, _the, _prior, _front, al, _image, <prev_im>x1369, _P, RI, OR, _, RE, PORT, :, _N, /, A, _Prov, ide, _a, _description, _of, _the, _find, ings, _in, _the, _radi, ology, _study, _in, _comparison, _to, _the, _prior, _front, al, _image,., _IN, D, ICATION, :, __, _year, _old, _woman, _with, _rec, urrent, _asp, iration, _p, na, __, _now, _with, _f, lare, _in, _s, put, um, __, _c, ough, __, _and, _bil, ater, al, _lower, _lo, be, _crack, les, _//, _assess, _for, _new, _p, neum, onia, _TE, CH, NI, QUE, :, _Ch, est, _radi, ograph,., _PA, _and, _later, al, _views, _CO, MP, AR, I, SON, :, _Thus, _radi, ograph, __, __, _A, SS, IST, ANT, :, _Bil, ater, al, _lower, _lo, be, _op, ac, ities, _are, _improved, _compared, _to, __, __, _There, _are, _small, _co, ales, c, ence, _into, _several, _nod, ular, _op, ac, ities, _remaining, _on, _the, _right, _but, _mostly, _improved, __, _L, ungs, _are, _m, ild, ly, _hyper, infl, ated, __, _There, _is, _no, _definite, _ple, ural, _eff, usion, __, _Card, iom, ed, iast, inal, _sil, hou, ette, _is, _normal, _size, __, _2, _f, ract, ured, _sc, rew, s, _in, _right, _hum, eral, _head, _is, _un, changed, _from, _prior, __, </s></pre>	<pre>[start_index:end_index] message_type content_type [filtered tokens] [31:32] human str ['_image'] [1400:1401] human image ['<image>'] [1405:1406] human str ['_image'] [2774:2775] human image ['<lat_image>'] [2780:2781] human str ['_image'] [4149:4150] human image ['<prev_im>'] [4150:4160] human str ['_P', 'RI', 'OR', '_', 'RE', 'PORT', ':', '_N', '/', 'A'] [4182:4226] human str ['_IN', 'D', 'ICATION', ':', '__', '_year', '_old', '_woman', '_with', '_rec', '_curr', '_asp', 'iration', '_p', 'na', __, '_now', '_with', '_f', 'lare', '_in', '_s', 'put', '_um', __, '_c', 'ough', __, '_and', '_bil', 'ater', '_al', '_lower', '_lo', 'be', '_crack', '_les', '_//', '_assess', '_for', '_new', '_p', 'neum', 'onia'] [4226:4241] human str ['_TE', 'CH', 'NI', 'QUE', ':', '_Ch', 'est', '_radi', 'ograph', __, '_PA', '_and', '_later', '_al', '_views'] [4241:4251] human str ['_CO', 'MP', 'AR', 'I', 'SON', ':', '_Thus', '_radi', 'ograph', __] [4257:4344] assistant str ['_Bil', 'ater', '_al', '_lower', '_lo', 'be', '_op', 'ac', 'ities', '_are', '_improved', '_compared', '_to', __, __, '_There', '_are', '_small', '_co', 'ales', 'c', 'ence', '_into', '_several', '_nod', 'ular', '_op', 'ac', 'ities', '_remaining', '_on', '_the', '_right', '_but', '_mostly', '_improved', __, '_L', 'ungs', '_are', '_m', 'ild', 'ly', '_hyper', 'infl', 'ated', __, '_There', '_is', '_no', '_definite', '_ple', 'ural', '_eff', 'usion', __, '_Card', 'iom', 'ed', 'iast', 'inal', '_sil', 'hou', 'ette', '_is', '_normal', '_size', __, '_2', '_f', 'ract', 'ured', '_sc', 'rew', 's', '_in', '_right', '_hum', 'eral', '_head', '_is', '_un', 'changed', '_from', '_prior', __]</pre>
Total # tokens = 4348	Total # filtered tokens = 176

A.2. SAE Hyperparameters

Table A.2 shows all the hyperparameters that were overridden from the default values in the `dictionary_learning` repository⁶.

We realised we had accidentally run with reversed Matryoshka group sizes, with the largest group being ‘innermost’. This appears to have slightly reduced the overall interpretability of the discovered features. We will quantify the impact on steering in a revision. However, given we do not see a strong association between interpretability score and steering success on the feature level, we do not expect a significant difference in our findings.

Table A.2. Hyperparameters used for training the SAE using the open-source repository `dictionary_learning`.

Category	Value	Description
<i>SAE Configuration</i>		
Type	<code>matryoshka_batch_topk</code>	Type of SAE architecture used.
Activation dimension	4096	The dimensionality of the activations in the SAE model.
Expansion factor	8	The factor by which the number of dictionary atoms is expanded.
Layer ID	15	The specific layer from which the embeddings are extracted.
Hookpoint	<code>residual</code>	The hookpoint in the model from where embeddings are captured.
k (active features)	256	The number of active features in the sparse encoding.
Group fractions	[1/2, 1/4, 1/8, 1/16, 1/16]	The fractions used to group dictionary atoms, controlling the sparsity levels at different scales.
<i>Trainer Configuration</i>		
Epochs	1	The number of training epochs.
Learning rate	Auto	The learning rate is automatically set by the trainer.
Aux k alpha	0.03125	The weight of the auxiliary k -sparse loss term.
Threshold beta	0.999	The exponential decay rate used for thresholding.
Threshold start step	1000	The step at which thresholding begins during training.
Threshold dead features	100000	The number of tokens after which a feature without activation will be considered “dead” (used in the auxiliary loss).
<i>Data Configuration</i>		
Batch size	8192	The number of samples in each batch for training.
Normalize activations	True	Whether or not to normalize the activations to unit norm.

A.3. Auxiliary Loss

As introduced by Gao et al. (2024), the auxiliary loss \mathcal{L}_{aux} captures the reconstruction error associated with the top- k_{aux} dead nodes in the sparse latent space. It is defined as:

$$\mathcal{L}_{\text{aux}} = \|e - \hat{e}\|_2^2, \quad (3)$$

where $e = x - \hat{x}$ is the error from the main model, and $\hat{e} = W_{\text{dec}}^k z$ represents the reconstruction obtained using the top- k_{aux} dead latents. A latent is considered “dead” if it has not activated for a predefined number of tokens, as specified by the threshold dead features.

⁶https://github.com/saprmarks/dictionary_learning

B. Feature statistics

Figure B.1 provides statistics on the activation frequency of features in the studied SAE, using a random sample of 500,000 data points from the training set. Each sample here refers to the model representation extracted at a single token position.

Defining the feature density as the fraction of samples on which a given feature activates, we observe (Figure B.1; top left, top middle) a range of values, with a very small number of features activating on almost all samples. Unfortunately, these commonly-occurring features are not well-explained: f_{7633} activates on 99.3% of samples and achieves $F_1 = 0.40$, f_{6727} activates on 86.8% of samples and is described as ‘*Detailed comparison with prior images highlighting interval changes.*’ with $F_1 = 0.67$. We did not observe a correlation between feature density and interpretability (detection F_1), however some of the most interpretable features have low density - f_{13515} ($F_1 = 0.97$, ‘*Elevation of the hemidiaphragm.*’) activates on only 159 samples (0.03%).

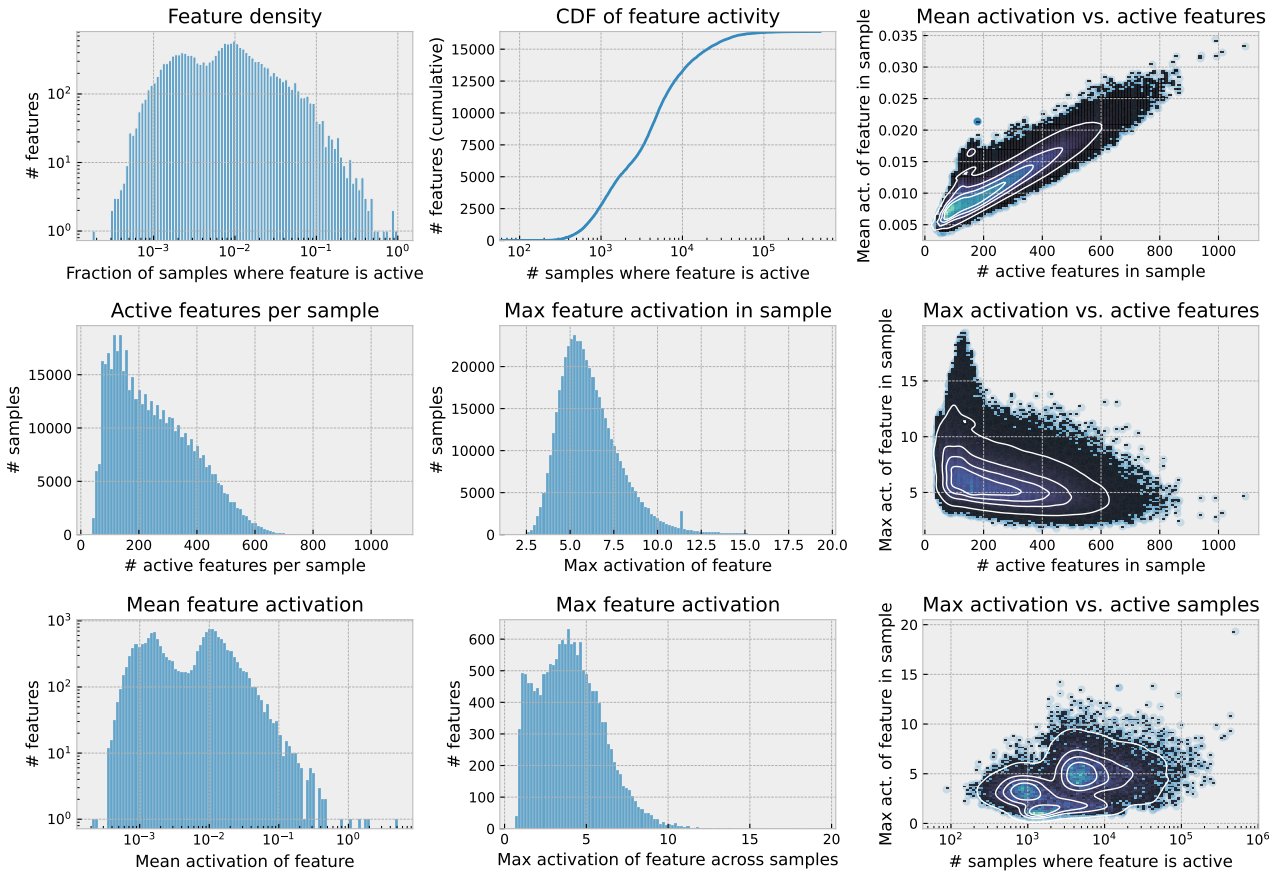


Figure B.1. Statistics on the activation frequency and strength of features in the studied SAE, using a random sample of 500,000 data points from the training set. Each sample here refers to a single token position.

C. Automated interpretability

We split the dataset 50:50 by patient into ‘train’ and ‘evaluation’ for the purpose of generating and scoring latent interpretations respectively. We consider each latent individually. We use GPT-4o (2024-11-20) via the Azure OpenAI service. Initial experiments with o3-mini (2025-01-31) yielded inferior results, but may benefit from further prompt engineering.

C.1. Selecting and preparing feature exemplars

For each feature, we select ‘exemplar’ data samples by selecting an equal number of non-activating and activating samples, for a total of 50. Activating samples are selected from the top decile of the feature activation distribution, treating an

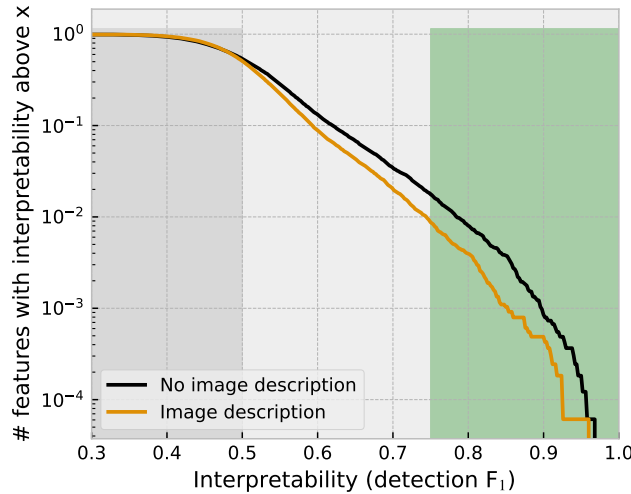


Figure C.1. Including the ‘description’ of the image (‘Findings’ section of the report) to the interpretation LLM does not increase the number of interpretable features we discover.

activation of 0 as the bottom decile. Experiments with stratified sampling indicated this strategy was marginally superior.

Each data sample refers to a specific token index for a specific input sequence. To explain the feature activation at that point, we provide the LLM with the full sequence up to that token, and the next 100 characters. We indicate the ‘current’ token with double square brackets. We found that truncating to 100 characters after the current token provided slightly improved interpretability scores relative to truncating to 0, 10, or 250 characters. Note that our few-shot examples, being hand-designed, inconsistently adhere to the truncation length.

Since MAIRA-2 is a MLLM, it receives interleaved images and text as input. Our interpretation LLM is text-only, we replace the image tokens with the string ‘<image>’. In a chest X-ray report, the ‘Findings’ section of the report approximates a description of the image. We experimented with including this section prefixed to the data sample, to provide the LLM with information about the image contents. Surprisingly (Figure C.1), we found this did *not* improve the number of interpretable features we could discover. We note however that we train the SAE (and hence interpret it) on both the prompt and target tokens used for MAIRA-2 training, where the training target is the ‘Findings’ section. Hence, in many cases the input text to the model may already contain some part of the image description.

C.2. Generating interpretations

We use a modified prompt based on [Paulo et al. \(2024\)⁷](#). For each example, we present a single latent activation, scaled to 0-9 based on the range of observed values of that latent, following [Gao et al. \(2024\)](#).

The instruction provided to the explanation-deriving LLM is shown below:

Latent interpretation: system message

You are a meticulous AI researcher conducting an important investigation into the activation patterns of a large autoregressive vision-language model trained on chest X-ray data. You will be presented with samples of prompts to and outputs from this model with corresponding activation levels at a specified token. Your task is to analyze this data and provide an explanation which succinctly encapsulates patterns to explain the observed activation levels.

Guidelines:

- Each data example consists of some preamble text, the [[current token]], and the next few tokens, as well as an “activation level” computed at the [[current token]]. Note that the current token is delimited with “[,]”.

⁷https://github.com/EleutherAI/delphi/tree/article_version

- The activation level indicates how representative the sample is of the pattern we wish to understand.
- Activation levels close to zero mean the pattern is NOT present.
- These examples can refer to "<image>". In this case, an <IMAGE_DESCRIPTION> may be provided.

Produce the SHORTEST and MOST CONCISE explanation of the pattern, with a rationale.

Respond in JSON with the following fields:

```
{
  "rationale": "Justification for this explanation.",
  "explanation": "Concise explanation of the pattern."
}
```

We use six few-shot examples based on our medical use-case, devised in conjunction with Claude 3.7 Sonnet Thinking. Each example features samples from a hypothetical latent with different activation levels. We tried to design few-shots to cover possible latents including those pertaining to pathologies or other image-specific concepts, as well as 'meta' concepts such as the length into the input sequence (as described by [Gao et al. \(2024\)](#)), and 'superficial' concepts such as the appearance of a specific token.

We present one below:

Latent interpretation: illustrative few-shot example

Input:

Example 1: [[_IN]]DICATION: 58-year-old female with persistent cough. FINDINGS: No acute cardiopulmonary process. Heart size is normal.

Activation: 8

Example 2: TECHNIQUE: PA and lateral chest radiographs were obtained. [[The]] cardiac silhouette appears normal in size.

Activation: 0

Example 3: EXAMINATION: Chest CT. [[_IN]]DICATION: Follow-up for previously identified pulmonary nodule. FINDINGS: Left lung is clear, nodule persists in right lower lobe. No new masses identified.

Activation: 7

Example 4: The patient presents with shortness of breath and chest pa[[_in]]. No fever reported.

Activation: 0

...

Output:

```
{
  "rationale": "The activation is high when '_IN' appears as the first token of the 'INDICATION' section, but is not high when '_IN' appears in other contexts.",
  "explanation": "The token '_IN' appearing as part of the word 'INDICATION'"
}
```

C.3. Scoring interpretations

We follow the detection scoring approach outlined by [Paulo et al. \(2024\)](#), and again draw inspiration from the prompts used in that study. The LLM is provided with the interpretation of a latent (a sentence) and a sample. It is asked to classify whether the latent would activate on that sample.

Below we show the system message:

Interpretation scoring: system message

You are an intelligent and meticulous researcher into clinical language, with a specialisation in radiology.

You will be provided with a "latent explanation", which describes a "latent property" of the text (a concept or pattern which can appear in text), such as "patient deterioration" or "mention of

lung opacities".

You will then be given several text examples. Your task is to determine which examples possess latent property. These examples may appear to have truncated text. Regardless of the formatting, focus on determining whether the text has the property in the "latent explanation".

For each example, return 1 if the example demonstrates the property, and 0 otherwise.

Again we devised few-shot examples in conjunction with Claude 3.7 Sonnet Thinking. Using a small development dataset, we found that the LLM performed better on the task when it was asked to classify a single sample at a time, however few-shot examples included several samples at once. An illustrative case is shown below:

Interpretation scoring: illustrative few-shot example

Input:

Latent explanation: Comparison with prior imaging studies.

Test examples:

Example 0: Chest radiograph demonstrates bibasilar atelectasis with small bilateral pleural effusions. Heart size is upper limits of normal.

Example 1: Interval development of small right pleural effusion not present on prior chest radiograph performed 2 days ago.

Output:

[0, 1]

D. Automated steering evaluation

Our automated evaluation of steering success is implemented using a LLM judge similar to [Wu et al. \(2025\)](#). The model is prompted to provide a score from 0 to 1 for on-target changes and off-target changes and to reason about its decision beforehand. The LLM judge is then provided with ten few-shot examples of the task. We use individual system messages and few-shot examples for positive and negative steering. Similar to the automated interpretability pipeline (c.f. Appendix C), we use GPT-4o (2024-11-20) via the Azure OpenAI service.

Below we show the system message.

Automated Steering Evaluation: system message

You are an intelligent and meticulous researcher into clinical language, with a specialisation in radiology.

You will be provided with a "concept", which describes a concept or pattern which can appear in text, such as "patient deterioration" or "mention of lung opacities".

You will further be provided with two text samples:

1. A findings section of a radiology report (called "original")
2. A modified version of that section (called "modified")

You will then be given several text examples. Please act as an impartial judge and determine (1) to which degree the modified version is changed to `{{MODIFIER}}` better represent the concept compared to the original version ("on_target_score") and (2) to which degree the rest of the report stayed unchanged compared to the original version ("off_target_score").

Focus solely on the changes in information, without regard for different ways of representing the same information (e.g. reordering, different wording, etc.). Changes in relation to the concept should NOT be counted to the "off_target_score". Report both scores on a scale from 0 to 1 where 0 means no change

and 1 means strong changes.

Respond in JSON with the following fields:

```
{
  "on_target_score_reasoning": <reasoning for on_target_score>,
  "off_target_score_reasoning": <reasoning for off_target_score>,
  "on_target_score": <score between 0 and 1>,
  "off_target_score": <score between 0 and 1>
}
```

The value of `{{MODIFIER}}` in the system message depends on the steering direction and equals to “better represents” and “SUPPRESS” for steering in the positive and negative direction, respectively.

To calibrate the scores, few-shot examples are provided. An illustrative case is shown below with on-target changes between the original and the modified report highlighted in **green**, and off-target changes highlighted in **orange**.

Automated Steering Evaluation: illustrative few-shot example

Original report: Cardiac size is within normal limits. The lungs are clear **without focal consolidation**, pleural effusion, or pneumothorax.

Modified report: Cardiac size is normal. **The aorta is tortuous.** The lungs are clear. There is no pneumothorax or pleural effusion.

Concept: Increased tortuosity or calcification of the thoracic aorta.

Output:

```
{
  "on_target_score_reasoning": "The modified report contains the concept in the statement \"The aorta is tortuous.\\". However, it doesn't mention an increase.",
  "off_target_score_reasoning": "The explicit mention of the absence of focal consolidation is omitted in the modified report.",
  "on_target_score": 0.7,
  "off_target_score": 0.2
}
```

E. Feature steering

In this section, we provide further results on feature steering and outline the selection process of features for these experiments.

E.1. Selection of features for steering

Since steering and its evaluation is computationally expensive, we select only a subset of features for this experiment. Since steering evaluation relies on a meaningful description of a feature, we start with an initial selection of features with $F_1 > 0.85$. Based on early results that indicate higher steering success of features that activate frequently in the training data, we manually add more such features, again focussing on ones with high F_1 -scores. These 74 features are depicted in Table E.1. Our objective here was to find the best-case scenario for steering to understand whether it is possible, hence iteratively searching for steerable features.

To obtain the final set of features for the steering task, we then remove findings that are not ‘output’ features (Paulo et al., 2024) (e.g. f_{1420} ‘Radiology description with COMPARISON noted as ‘None’’), and features describing low lung volumes. The steering evaluation results for the resulting set of 67 features are shown in Figure E.1 with corresponding examples in Table E.2 for positive steering and Figure E.2 and Table E.3 for negative steering.

For the analysis of the correlation between the activation frequency and on-target / off-target scores in Section 4.2, we did not include the manually added highly activating features to avoid further bias than the one induced by restricting the steering analyses to highly interpretable features ($F_1 > 0.85$). This resulted in 50 samples for this analysis. Due to the low

sample size, we used a permutation test with 9,999 permutations to check for statistical significance.

E.2. Detailed feature steering results

Table E.1: Feature explanations, their validation F_1 scores, and number of active samples, grouped by common themes.

Group	ID	F_1	# Active	Explanation
Medical devices	f_{8806}	0.86	1609	Reports detailing implanted device positions and termination locations.
	f_{516}	0.85	10639	Emphasis on device placement or termination sites in radiology studies.
	f_{9995}	0.85	831	Pacemaker presence and description in chest imaging reports.
	f_{12062}	0.95	1028	Presence or repositioning of pigtail catheters in chest imaging.
	f_{11240}	0.94	1365	Descriptions of findings related to chest tube placement or removal.
	f_{10736}	0.86	1059	Change or removal of tubes or lines on imaging.
	f_{11427}	0.86	3109	Evaluating interval changes post-removal of chest tubes or medical devices.
	f_{9561}	0.86	2090	Detecting changes post chest tube removal, particularly pneumothorax assessment.
	f_{13086}	0.90	665	Reported precise distances for tubes from anatomical landmarks (e.g., carina).
	f_{10223}	0.88	2908	Focus on the placement and position of PICC lines in the SVC or atrium.
	f_{8582}	0.87	762	Reports on tube placement and adjustment recommendations.
	f_{12702}	0.86	329	Assessing and reporting the position of tubes in relation to anatomical landmarks like the carina.
	f_{437}	0.86	24497	Focus on descriptions of positions and placements of medical devices or lines.
	f_{10629}	0.86	1947	Precision in tube placement description.
	f_{11384}	0.86	611	Focus on tube or line placement positioning.
	f_{9002}	0.85	5615	Describes placement or adjustment necessity of medical tubes or catheters.
	f_{12355}	0.87	4912	Focus on endotracheal tube position and monitoring devices.
	f_{8757}	0.92	420	Central line or catheter placement described with specific position (e.g. 'mid SVC').
	f_{14399}	0.88	360	Changes in Swan-Ganz catheter placement and position.
	f_{9328}	0.91	2687	Describes postsurgical changes after lung surgeries.
	f_{13592}	0.96	416	Presence and mention of surgical clips in the imaging reports.
	f_{12150}	0.90	1040	Presence of surgical clips in imaging unrelated to main findings.
	f_{14168}	0.87	816	Presence of suture material or surgical changes in lung fields.
	f_{13375}	0.85	1188	Presence of stents or vascular devices in chest imaging comparison.
	f_{14905}	0.85	415	Intact median sternotomy wires noted in findings.
	f_{3037}	0.84	25498	Descriptions of medical device positioning relative to anatomy, often compared to prior images.
	f_{5156}	0.83	10791	Evaluation of medical device placements and changes.
	f_{2475}	0.83	11692	Precise positioning or placement of medical devices in radiological reports.
	f_{65}	0.83	10219	Focus on placement and position of tubes and lines in radiological findings.
	f_{3246}	0.80	27373	Evaluation of pacemaker or ICD lead positions in chest X-rays.
	f_{5791}	0.75	13374	Analysis and repositioning of Dobbhoff tube placement.
	f_{1729}	0.80	11306	Assessment and positioning of endotracheal tubes.
Abnormal findings	f_{13963}	0.94	258	Attributes suggestive of chronic obstructive pulmonary disease (COPD).
	f_{12585}	0.93	322	Unfolded or tortuous thoracic aorta in radiology reports.
	f_{13113}	0.87	478	Unfolding or tortuosity of the thoracic aorta.
	f_{1336}	0.86	11796	Aortic tortuosity or calcification identified in chest imaging.
	f_{14586}	0.94	533	Presence of plate-like or linear atelectasis.
	f_{1374}	0.88	3349	Presence of atelectasis in imaging findings.
	f_{6105}	0.88	3109	Mentions and descriptions of atelectasis.
	f_{14427}	0.86	443	Retrocardiac opacification or atelectasis indicating volume loss or infection.
	f_{11555}	0.93	401	Detection of calcified structures in radiological findings.
	f_{9958}	0.89	602	Atherosclerotic calcifications noted at the aortic knob or thoracic aorta.
	f_{12236}	0.89	656	Presence of aortic arch calcifications or related cardiac calcifications.
	f_{4875}	0.86	4444	Cardiomegaly or enlarged cardiac silhouette.
	f_{6108}	0.86	11089	Findings of pulmonary vascular congestion or pulmonary edema.
	f_{13199}	0.92	302	Emphysema-related findings or descriptors.
	f_{11509}	0.89	1123	Observations of rib fractures in chest imaging reports.
	f_{13400}	0.89	630	Presence of pleural scarring or thickening, often unchanged, in radiology reports.
	f_{10636}	0.86	743	Blunting of costophrenic angles suggesting pleural effusion.
	f_{6412}	0.84	5922	Detection of pleural effusions on imaging studies.
	f_{13506}	0.90	486	Mention of scoliosis in radiological comparisons.
	f_{13515}	0.97	159	Elevation of the hemidiaphragm.
	f_{13911}	0.90	412	Elevation of the hemidiaphragm.

Table E.1: Feature explanations, their validation F_1 scores, and number of active samples, grouped by common themes (cont.).

Group	ID	F_1	# Active	Explanation
	f_{7458}	0.82	14739	Elevation of the hemidiaphragm on imaging studies.
	f_{13258}	0.86	3238	Presence of hiatal hernia and related structural effects.
	f_{1172}	0.84	19306	Cardiomegaly or heart enlargement observations in chest imaging.
	f_{6987}	0.78	55984	Cardiopulmonary findings suggesting congestion, cardiomegaly, or pleural effusion.
	f_{6343}	0.80	40032	Low lung volumes increasing broncho-vascular markings or heart silhouette.
	f_{2883}	0.76	45007	Changes or stability in pneumothorax or pneumomediastinum over time compared to prior studies.
Normal findings	f_{11891}	0.87	1374	Normal imaging findings with emphasis on absence of acute pathology.
	f_{10709}	0.87	1761	Findings indicate clear lungs with no signs of pleural effusion, pneumothorax, consolidation, or pulmonary edema.
	f_{8735}	0.85	949	Clear lungs, no pleural effusion or pneumothorax, unremarkable cardiac and mediastinal silhouettes.
	f_{10234}	0.85	1347	Clear lungs with no focal consolidation, effusion, or pneumothorax.
Temporal changes	f_{9876}	0.86	800	Comparison with prior images and mention of healed rib fractures.
	f_{1646}	0.79	30532	Interval change in disease findings from prior imaging.
	f_{1599}	0.79	98759	Describing findings without comparison to prior images.
	f_{6150}	0.75	135961	Reports describe interval changes in medical devices or effusions compared to prior images.
Textual features	f_{6907}	0.91	5185	Presence of double-bracketed image tags [[<image>]].
	f_{12106}	0.88	660	Use of 'however' in clinical findings indicating possible issues needing further investigation.
	f_{7433}	0.88	5661	Prominent images marked by double brackets [[<image>]] in descriptions.
	f_{9473}	0.86	677	Use of 'possible' or 'possibly' indicating uncertainty.
	f_{10643}	0.86	999	Immediate notification of findings by telephone upon discovery.
	f_{11088}	0.76	719	No prior images available ('N/A') for comparison in the context.
	f_{3716}	0.72	2466	Presence of 'shortness of breath' as an indication.
	f_{9272}	0.72	883	Use of 'congestion' in radiology findings.

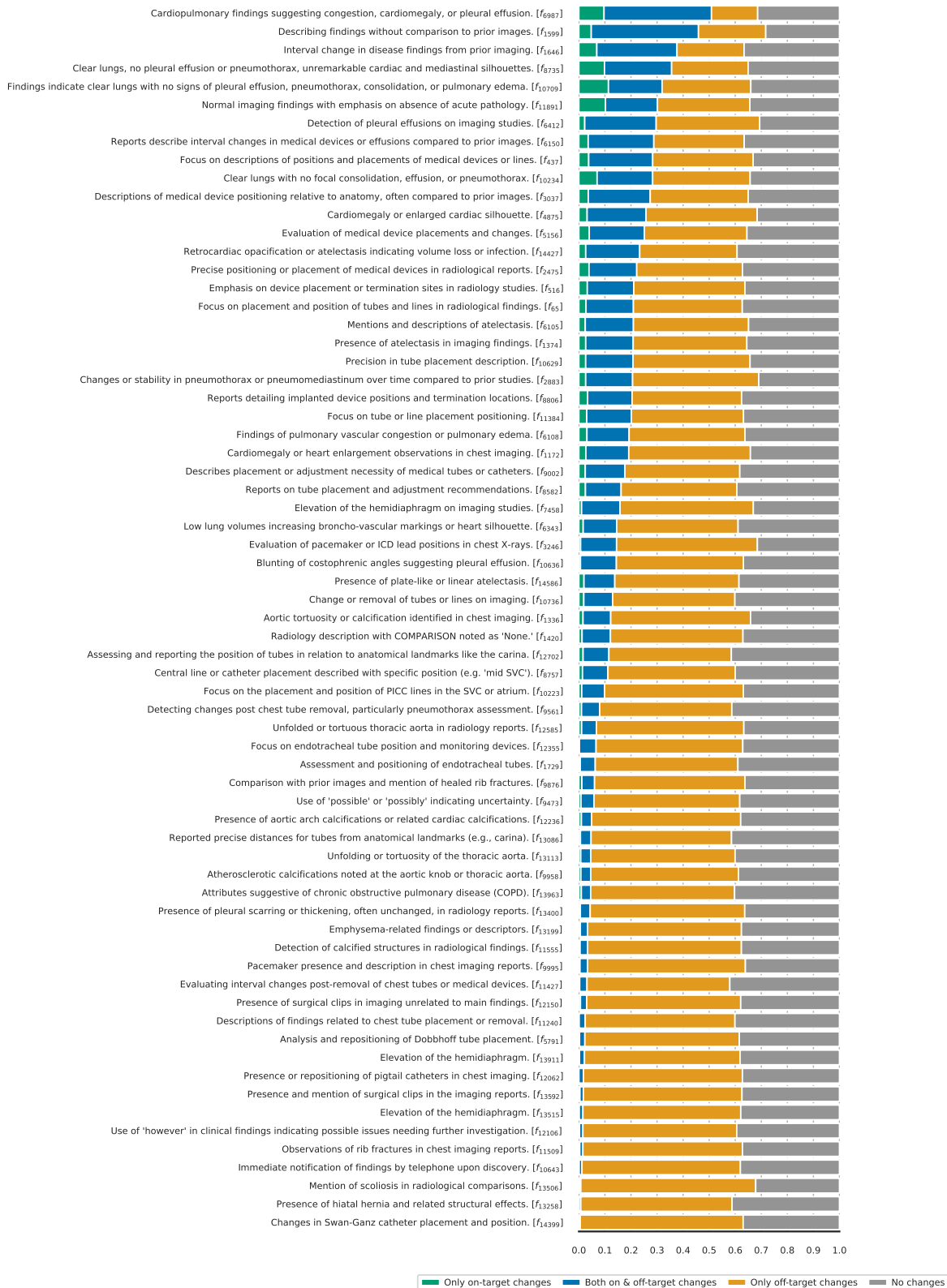


Figure E.1. Evaluating success of steering with $\alpha = 10$ for all steered features. Proportions of pure *on-target changes*, *off-target changes*, the combination of the two and no changes at all. The results of the automatic steering evaluation are binarised for this plot. Scores > 0.1 count as changes.

Table E.2. Additional examples of steered reports including evaluation. On-target changes between the original and the steered report are highlighted in **green**, off-target effects in **orange**. The subtitle colours match the corresponding bars in Figure E.1

Only on-target changes	
Feature	$f_{1646}, F_1 = 0.79$: 'Interval change in disease findings from prior imaging.'
Original	The heart size is mildly enlarged. The mediastinal contours are unremarkable. There is mild pulmonary vascular congestion. Small bilateral pleural effusions are noted. No pneumothorax is identified. There are no acute osseous abnormalities.
Steered $\alpha = 10$	The heart size is mildly enlarged. The mediastinal contours are unremarkable. There is mild pulmonary vascular congestion, slightly worse when compared to the prior study . Additionally, small bilateral pleural effusions are new compared to the prior exam . No focal consolidation or pneumothorax is identified. There are no acute osseous abnormalities.
Scores	on-target score=1.0 off-target score=0.0
Feature	$f_{10709}, F_1 = 0.87$: 'Findings indicate clear lungs with no signs of pleural effusion, pneumothorax, consolidation, or pulmonary edema.'
Original	There is a new opacity in the right mid lung, which is concerning for pneumonia. The cardiac, hilar and mediastinal contours are normal. No pleural abnormality is seen.
Steered $\alpha = 10$	The lungs are clear. The cardiac, hilar and mediastinal contours are normal. No pleural abnormality is seen.
Scores	on-target score=1.0 off-target score=0.0
Both on- and off-target changes	
Feature	$f_{6105}, F_1 = 0.88$: 'Mentions and descriptions of atelectasis.'
Original	AP and lateral views of the chest. The lungs are hyperinflated but clear of consolidation. There is no effusion. Cardiomedastinal silhouette is within normal limits. No acute osseous abnormality detected.
Steered $\alpha = 10$	PA and lateral views of the chest were provided. The lungs are hyperinflated, though there is no focal consolidation, effusion, or pneumothorax . There is a linear density in the right lower lung which is most compatible with atelectasis. Cardiomedastinal silhouette is stable . Bony structures are intact.
Scores	on-target score=1.0 off-target score=0.2
Feature	$f_{3246}, F_1 = 0.80$: 'Evaluation of pacemaker or ICD lead positions in chest X-rays.'
Original	A Port-A-Cath terminates in the superior vena cava. A nasogastric tube terminates in the stomach. The cardiac, mediastinal and hilar contours appear stable. There is no pleural effusion or pneumothorax. The lungs appear clear.
Steered $\alpha = 10$	A nasogastric tube terminates in the right atrium. A dual-lead pacemaker/ICD device appears unchanged. The heart is normal in size. The mediastinal and hilar contours appear stable. There is no pleural effusion or pneumothorax. The lungs appear clear.
Scores	on-target score=0.3 off-target score=0.7
Only off-target changes	
Feature	$f_{13506}, F_1 = 0.90$: 'Mention of scoliosis in radiological comparisons.'
Original	The cardiomedastinal and hilar contours are within normal limits. Lungs are well expanded and clear. There are no focal consolidations, pleural effusions, pulmonary edema or pneumothorax.
Steered $\alpha = 10$	The cardiomedastinal and hilar contours are within normal limits. There is evidence of calcified mediastinal and hilar lymph nodes consistent with known sarcoidosis. There is no focal consolidation, pleural effusion or pneumothorax. Sternotomy wires are intact.
Scores	on-target score=0.0 off-target score=0.5
Feature	$f_{14399}, F_1 = 0.88$: 'Changes in Swan-Ganz catheter placement and position.'
Original	The heart size is within normal limits. The mediastinal and hilar contours are normal. The lungs are clear. There is no pleural effusion or pneumothorax.
Steered $\alpha = 10$	The heart size is within normal limits. The mediastinal and hilar contours are also within normal limits. The lung volumes are low, but no consolidation , pleural effusion or pneumothorax is seen.
Scores	on-target score=0.0 off-target score=0.2

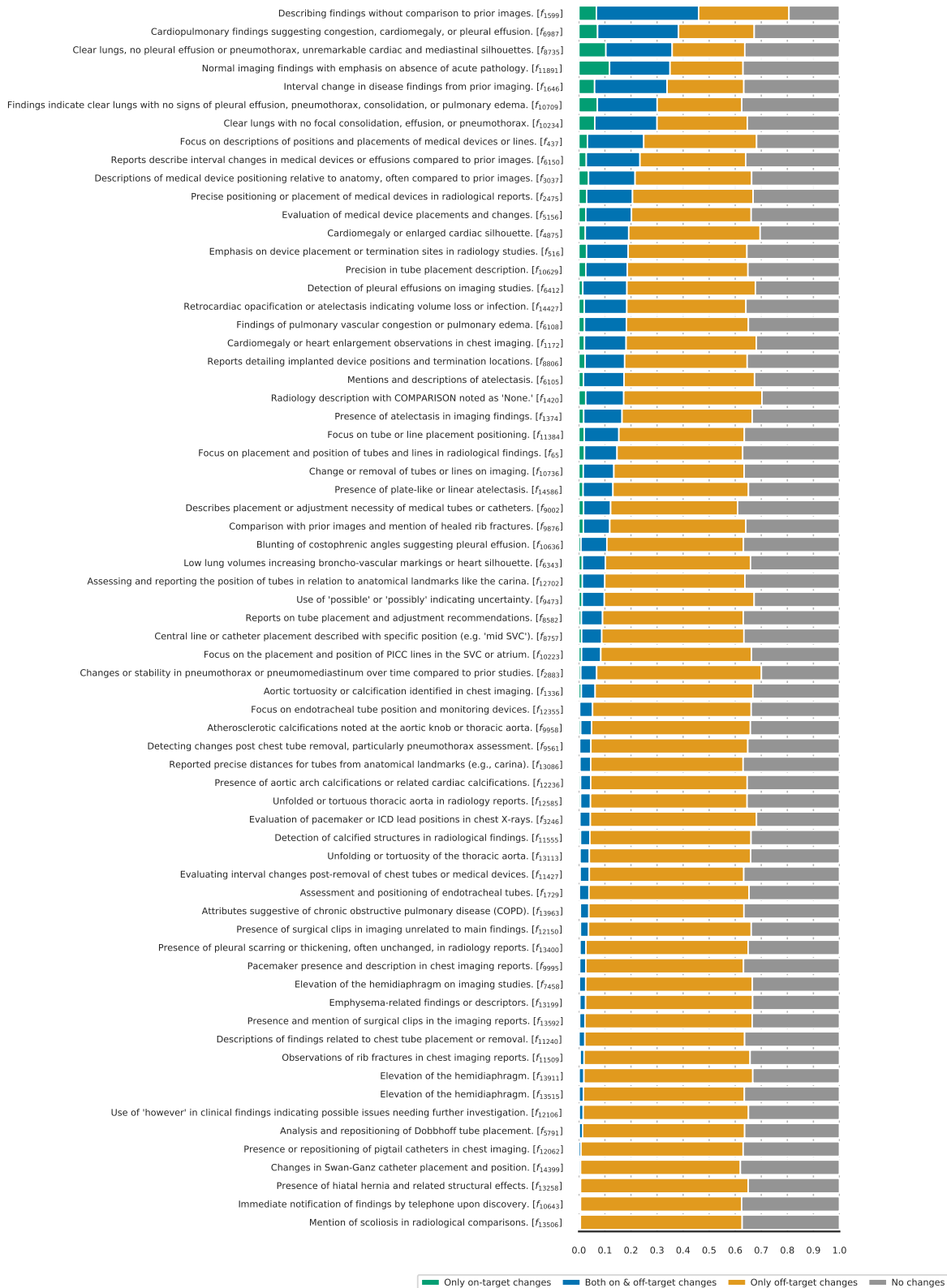


Figure E.2. Evaluating success of steering with $\alpha = -10$ for all steered features. Proportions of pure *on-target changes*, *off-target changes*, the combination of the two and no changes at all. The results of the automatic steering evaluation are binarised for this plot. Scores > 0.1 count as changes.

Table E.3. Additional examples of steered reports including evaluation. On-target changes between the original and the steered report are highlighted in green, off-target effects in orange. The subtitle colours match the corresponding bars in Figure E.1

Only on-target changes	
Feature	<i>f₆₉₈₇, F₁ = 0.78: 'Cardiopulmonary findings suggesting congestion, cardiomegaly, or pleural effusion.'</i>
Original	As compared to the chest radiograph from 1 day prior, right-sided pigtail catheter has been removed. No pneumothorax. Small right-sided pleural effusion has slightly increased. Mild pulmonary vascular congestion. Mild cardiomegaly.
Steered $\alpha = -10$	As compared to the chest radiograph from 1 day prior, right-sided pigtail catheter has been removed. No pneumothorax. The remaining appearance of the lungs is unchanged.
Scores	on-target score=1.0 off-target score=0.1
Feature	<i>f₁₆₄₆, F₁ = 0.79: 'Interval change in disease findings from prior imaging.'</i>
Original	The cardiac, mediastinal and hilar contours appear stable. There is no pleural effusion or pneumothorax. The lungs appear clear. Bony structures are unremarkable. There has been no significant change.
Steered $\alpha = -10$	The cardiac, mediastinal and hilar contours appear stable. There is no pleural effusion or pneumothorax. The lungs appear clear. Bony structures are unremarkable.
Scores	on-target score=1.0 off-target score=0.0
Both on- and off-target changes	
Feature	<i>f₆₁₀₅, F₁ = 0.88: 'Mentions and descriptions of atelectasis.'</i>
Original	Right small pleural effusion has improved since - with pigtail still in place. There is no pneumothorax. Left lower lobe atelectasis has improved. There is no new lung consolidation. Mediastinal and cardiac contours are normal.
Steered $\alpha = -10$	Right pigtail is no longer seen and there is no visible pneumothorax. The lungs are clear. The cardiac and mediastinal contours are unremarkable. There is no pleural effusion.
Scores	on-target score=1.0 off-target score=0.5
Feature	<i>f₂₄₇₅, F₁ = 0.83: 'Precise positioning or placement of medical devices in radiological reports.'</i>
Original	As compared to the previous radiograph, there is no relevant change. The external pacemaker is in constant position. There is no evidence of pneumothorax or other complication. No pleural effusions. No pneumonia. Moderate cardiomegaly without pulmonary edema.
Steered $\alpha = -10$	As compared to the previous radiograph, there is no relevant change. Left shoulder in situ. No pneumothorax. No pulmonary edema. No pleural effusions. No pneumonia.
Scores	on-target score=1.0 off-target score=0.3
Only off-target changes	
Feature	<i>f₉₉₉₅, F₁ = 0.85: 'Pacemaker presence and description in chest imaging reports.'</i>
Original	A left pectoral dual-lead cardiac pacemaker device is unchanged. The lungs are well expanded. No focal consolidation, edema, effusion, or pneumothorax. The heart is top-normal in size. The mediastinum is not widened. Aortic knob calcifications are mild.
Steered $\alpha = -10$	A left pectoral dual-lead cardiac pacemaker device is unchanged. The lungs are well-expanded. No focal consolidation, edema, effusion, or pneumothorax. The heart is top-normal in size. The mediastinum is not widened. The hila are unremarkable.
Scores	on-target score=0.0 off-target score=0.2
Feature	<i>f₁₂₅₈₅, F₁ = 0.93: 'Unfolded or tortuous thoracic aorta in radiology reports.'</i>
Original	As compared to the previous radiograph, there is no relevant change. No evidence of pneumonia or other acute lung disease. Minimal scars at the level of the right hilus. Known calcified granulomas in the right upper lobe. Mild tortuosity of the thoracic aorta. No pleural effusions. No pneumothorax.
Steered $\alpha = -10$	As compared to the previous radiograph, there is no relevant change. No evidence of pneumonia. Borderline size of the cardiac silhouette. Mild tortuosity of the thoracic aorta. No pleural effusions. No pneumothorax.
Scores	on-target score=0.0 off-target score=0.4